Ceramics International 51 (2025) 58287–58296

Contents lists available at ScienceDirect

Ceramics International

journal homepage: www.elsevier.com/locate/ceramint

3D printing of alumina components via Fused Granulate Fabrication technology and solvent-free debinding of highly filled feedstocks comprising (LD)-polyethylene and cellulose

Claudia Heuer [a,*], Benjamin Bock-Seefeld [a], Patricia Kaiser [a], Christian Weigelt [a], Piotr Malczyk [a], Nora Brachhold [a], Dimosthenis Trimis [b], Christos G.C. Aneziris [a]

[a] Technische Universität Bergakademie Freiberg, Institute of Ceramics, Refractories and Composite Materials, Agricolastraße 17, 09599, Freiberg, Germany
[b] Karlsruhe Institute of Technology (KIT), Engler-Bunte-Institut, Combustion Technology, Engler-Bunte-Ring 7, 76131, Karlsruhe, Germany

ARTICLE INFO

Handling Editor: P. Vincenzini

Keywords:
3D printing
Fused granulate fabrication
Pellets
Thermal debinding
Solvent-free debinding
Alumina

ABSTRACT

This study focuses on the development of components in gyroid structure based on alumina as integral part of the novel burner designed for the non-premixed combustion of ammonia. During application, the component has to withstand repeated thermal shocks of approx. 600 K or more. Due to the high geometric complexity of the gyroid structure and the need for lightweight design with both macroporous regions and microporous features only the 3D printing was suitable as manufacturing technology; in the present work Fused Granulate Fabrication was used. The manufacturing routine for the employed granules with special regard to the binder system is developed. A customized thermal debinding regime without wick or solvent debinding is presented. Challenges such as the formation of bubbles and the swelling of the samples during thermal debinding were met by adjusting the printing parameters to create porosity and cavities between the deposited strands during 3D printing. Sintered bars fabricated using optimized printing parameters had a shrinkage of 13 %, an open porosity of 41 % and a flexural strength of 50 MPa, respectively. These values are sufficient for the application of the components in the novel burners. As last part of this work sheet-gyroid structures were prepared using a 1.0 mm and 0.4 mm nozzles. These structures successfully survived 5 thermal shock cycles, each involving heating to 1100 °C followed by air quenching, which is an excellent result in terms of thermal shock performance.

1. Introduction

Additive Manufacturing (AM) technologies for the fabrication of ceramic components have become the focus of research & development and according to current forecasts manufacturers will soon be able to start serial production in a wide range of industries such as automobile, machine construction, aerospace and medical applications, thus increasing market demand and revenue [1]. With AM technologies complex geometries and internal structures can be easily manufactured and due to the combination of raw materials advantageous component properties (including graded structures) can be achieved. The AM processes are divided into three main groups: powder bed-based methods (e.g. selective laser sintering, binder jetting), suspension-based methods (e.g. stereolithography, digital light processing) and extrusion-based methods (e.g. fused filament fabrication (FFF), fused granulate fabrication (FGF)) [2]. In FGF 3D printing, granules are directly fed into the extruder unit installed in the printer, which eliminates the cost and time-consuming filament fabrication step, thus saving 60–90 % material costs. With FGF technology, old or defective 3D printed part can be shredded and reused in the printing process. The FGF technology requires a precise control and management of the material flow and there are still challenges in the fabrication of filigree components [3]. The extrusion-based methods often use a feedstock that consist of a multi-component polymer system and a ceramic filler material, which typically comprises ≥50 vol% of the feedstock. For the fabrication of advanced ceramics via 3D printing, very fine sub-micron sized powders are utilized. Nowadays, typical ceramic filler materials are alumina [4,5] and zirconia [6–8], but there are also various developments in terms

* Corresponding author.
E-mail addresses: claudia.heuer@ikfvw.tu-freiberg.de (C. Heuer), benjamin.bock@ikfvw.tu-freiberg.de (B. Bock-Seefeld), patricia.kaiser@ikfvw.tu-freiberg.de (P. Kaiser), christian.weigelt@ikfvw.tu-freiberg.de (C. Weigelt), piotr.malczyk@ikfvw.tu-freiberg.de (P. Malczyk), nora.brachhold@ikfvw.tu-freiberg.de (N. Brachhold), dimosthenis.trimis@kit.edu (D. Trimis), aneziris@ikfvw.tu-freiberg.de (C.G.C. Aneziris).

https://doi.org/10.1016/j.ceramint.2025.10.048
Received 3 April 2025; Received in revised form 22 August 2025; Accepted 3 October 2025
Available online 4 October 2025

of non-oxide ceramics such as silicon carbide [9] and silicon nitride [10].

In the extrusion-based printing processes, the thermoplastic material is melted and selectively extruded through a nozzle and deposited layer by layer to build the desired component [5,6]. The material to be printed is provided as filament (FFF) or granules/pellet (FGF) for the 3D printing process [4–6,11,12]. The granules/pellets are also the raw material for the fabrication of continuous filaments. This means an additional fabrication process with special filament extrusion equipment has to be employed for filament fabrication. In addition, various requirements are placed on the filaments such as sufficient strength and flexibility in order to ensure uniform feeding of the filament trough the extrusion unit without tearing as well as uniform deposition onto the printing bed without buckling or bending. Thus, the effort to fabricate and subsequently the prices for the filaments are significantly higher as compared to granules/pellets. For both types of feedstock thermoplastic binders such as acrylonitrile butadiene styrene (ABS), polylactic acid (PLA), polypropylene (PP), polyethylene (PE) and ethylene vinyl acetate (EVA) are used.

After printing, these binders have to be removed from the component before sintering. According to the state of the art, an initial chemical debinding step removes the main binder catalytically or using solvents (such as ethanol, acetone, ethylene acetate, cyclohexane or n-heptane) from the green component in order to create a certain porosity to enable a subsequent thermal debinding. The main binder is dissolved from the outside to the inside of the component (concentration gradient) and a porous brown part remains. The brown part consists of the ceramic particles as well a backbone polymer (used as dimensional stabilizer), which is subsequently removed by decomposition to gaseous components during the thermal debinding process. The contaminated solvent from the first chemical debinding step can be distilled and recycled. Although debinding with solvents is a common debinding routine for 3D printed components, there are major challenges in terms of human health, environmental protection and process engineering requirements. Therefore, it is essential to develop alternative debinding strategies for 3D printed components avoiding these drawbacks in order to establish 3D printing as a real alternative to conventional shaping technologies. The pure thermal debinding of large 3D FFF or FGF printed samples with typical binder contents ≥50 vol% still poses a challenge [13–18] and is currently not considered state of the art. At present, only thin-walled (up to 800 μm) and/or macro-porous components are debinded with a pure thermal treatment (no wick or solvent-based debinding).

The 3D FGF presents a highly interesting approach for the fabrication of functional ceramic components in high temperature applications, particularly with regard to their performance under recurring thermal shock. In high temperature applications, in which the materials have to survive sudden temperature changes of several 100 K during service, typically coarse-grained components (μm to mm scale, depending on component) with an open porosity of up to 20 % in the microstructure are employed in order to guarantee the needed thermal shock resistance. Using FGF technology, thin-walled, fine-grained refractory components can be manufactured layer-by-layer. Within a single component, both dense and macro-porous regions (pore size up to several mm) can be tailored during the printing process with the aim to meet the specific functional requirements. The fabrication of light-weight hollow structures does not only mean that lesser material is required, but also that temperature equilibrium under thermal loading is achieved easier. Furthermore, the thin-walled (thickness of few mm), layer-by-layer design with fine micropores (in μm range) can lead to a significant reduction in crack propagation energy [19]. An example for an application of 3D FFF printed components are spinel-based model nozzles for the casting of steel [20].

The present study deals with the development of components in gyroid structure based on alumina. Alumina is a highly stable ceramic material with a melting point of approx. 2040 °C. It is widely used as refractory materials and is suitable for application in ammonia and hydrogen atmospheres [21–23]. These components in gyroid structure [24] will be integral part of novel burners designed for the non-premixed combustion of ammonia [25]. Within the intertwined channels, ammonia and air are transported separately without pre-mixing; they are preheated due to thermal radiation and heat conduction. As integral part of the novel burner, the gyroid structure must withstand repeated thermal shocks of approx. 600 K or more. Due to the high geometric complexity of the gyroid structure component and the need for light-weight design with both microporous regions and microporous features only the 3D printing is suitable as manufacturing technology.

Within the present study, the optimal composition of the binder system and influence of the alumina powder with a mean particle size >4 μm was investigated. Printing parameters such as printing temperature and speed, line width and height were evaluated to identify the most suitable settings for a pure thermal debinding of printed parts. Within this study, the debinding regime was developed for rods and plates and was then transferred to gyroid structures with diameter of 50 mm and a height of 25 mm as well as to rectangular gyroid components with an edge length and height of 30 mm. Finally, the thermal shock performance of the gyroid structured components was evaluated by quenching the samples from 1100 °C to room temperature five times using compressed air.

2. Experimental part

The ceramic powder used in this study was a Tabular alumina (T60/64, Almatis, Germany) with a d_{50} = 4.33 μm, a d_{90} = 13.61 μm and a specific surface area of 3.32 m^2/g. The main binder components were two low density polyethylene (LDPE, Rowak AG, Germany) powders with the specification H70 (melting range: 100–104 °C) and H150 (melting range: 98–102 °C). These were mixed in a ratio H70: H150 of 62.5 : 37.5 vol% [20,26] to obtain a theoretical MFI (melt flow index) of 100 g/10 min according to the rule of mixture. Stearic acid (Sa, ≥98 %, Carl Roth, Germany) as well as ammonium-lignin sulfonate (C12C, Otto Dille, Germany) were used as surfactants. Cellulose powder (Sigma-Aldrich, Germany) served as backbone during thermal processing. The ratio of alumina to binder system was kept constant throughout the entire study. Generally, for classic 3D printing with polymers only, an MFI of 100 g/10 min would not be suitable since the material would have a very low viscosity. For the preparation of feedstocks that include ceramic powder, cellulose, etc. and in which the LDPE is only one part in the binder formulation it is suitable, that the MFI of LDPE is 100 g/10 min. Due to the filling of the binder matrix with ceramic particles, the viscosity increases strongly. Fig. 1 schematically illustrates the different compositions investigated within this study. In order to evaluate the influence of the cellulose on the dimensional stability of printed parts during thermal treatment, the cellulose content was varied from 10 to 20 vol%. Consequently, the polyethylene content (main component) was reduced from 79 vol% to 69 vol% to keep the binder content of the feedstock constant. The composition with 10 vol% cellulose, 15 vol% cellulose and 20 vol% cellulose are hereinafter referred to AT-***10***Cel-10Sa, AT-***15***Cel-10Sa and AT-***20***Cel-10Sa, respectively. The suitability of the various compositions for thermoplastic processing were screened using a Brabender measuring mixer type W 350 EHT (Brabender, Germany). The maximum volume of the mixing chamber was 370 cm^3 and the processing temperature was set to 133 °C. The torque was registered as a function of time.

The fabrication of the thermoplastic masses and thus the pellets/granules comprised several steps. The raw materials were pre-mixed in an Eirich laboratory mixer EL-1 (Maschinenfabrik Gustav Eirich, Germany) at room temperature for 300 s at 500 rpm. The thermoplastic processing was conducted in a single screw extruder with kneading equipment type LK III 2A (Linden, Germany) at 20 rpm and temperatures of 134 ± 2 °C. The pre-mixed raw materials were added stepwise into the kneader in order enable constant temperature conditions. The total mixing time was set to 30 min for all compositions. The

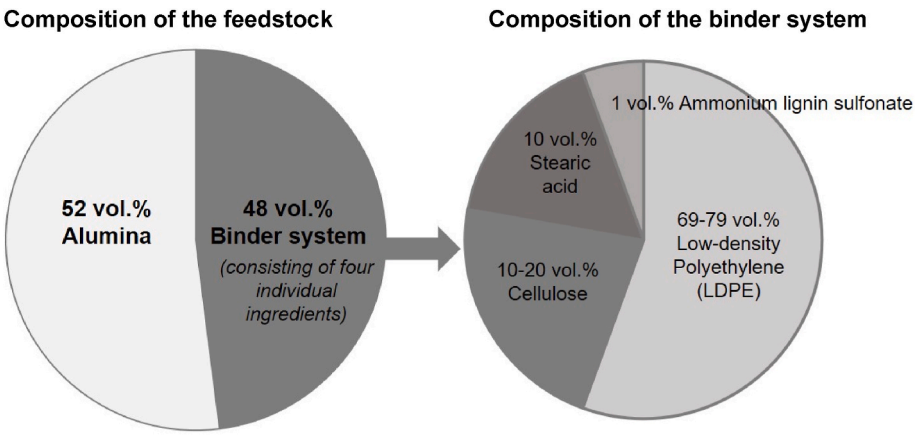

Fig. 1. Scheme of the investigated compositions.

thermoplastic masses were extruded to strands having a diameter of 3 mm using a die with 8 channels. The strands were manually cut into a length of 3–5 mm. Bars (4 × 5 × 60 mm^3) and plates (15 × 80 × 2.4 mm^3) as well as cylinders (diameter of 50 mm and height of 25 mm) with gyroid infill were designed using AutoDesk Fusion 360. Sheet-gyroid structures were generated using the software MSLattice [27] with a size of 2 × 2 × 2 cells, a relative density of 30 % and a mesh density of 30 points. A side wall construction was added using the software FreeCAD 0.21.2 [28]. The dimensions of the construction were 31.2 × 31.2 × 30 mm^3 (width x length x height) with a side wall thickness of 0.6 mm. The obtained stl.-files were translated into. gcode-files using the open source software UltimakerCura (version 5.6.0., Ultimaker, Netherlands). The 3D printing was conducted using a M.A.T. (Multi Additive Technology) printer (3D Ceram, France) equipped with a single extruder and a building volume of 200 × 200 × 200 mm^3. In order to demonstrate the CNC machinability of the developed feedstock, cubes with an edge length of 18 mm were printed and machined using CNC in green state. The initial printing parameters of the M.A.T. printer are summarized in Table 1. The printing was *initially* carried out concentrically from *outside to inside* with two walls, 100 % infill and a flow of 20 mm/s to create a dense layout of the strand with sufficient overlap. The temperature of the bed was set to 60 °C in order to ensure proper adhesion of the sample to the printing bed during printing. Additionally, a 5 mm brim was printed. The printing nozzle had a temperature of 210 °C for the brim and the first sample layer and was then decreased to 200 °C.

In order to evaluate the influence of the cellulose content on the dimensional stability of the printed components, rods with a diameter of 3 mm and a length of 100 mm were prepared during extrusion. These rods were placed on alumina bars with a span of 60 mm. The deformation of the rods during thermal debinding was registered (according to the developed debinding regime). The thermal decomposition behavior of the binder system composed of LDPE, cellulose, stearic acid and ammonium lignin sulfonate between room temperature and 600 °C was investigated using differential scanning calorimetry (DSC) combined with thermo-gravimetric measurements (TG) using a NETZSCH STA 409 PC/PG (Netzsch, Germany). The sample mass was 21.960 mg in an alumina crucible. The heating rate was set to 10 K/min and the device was constantly flushed with synthetic air with a flow rate of 70 ml/min. The consolidation kinetics of the ceramic phase was studied using a dilatometer type NETZSCH DIL 402C (Netzsch, Germany) at a heating rate of 5 K/min to a maximum temperature of 1400 °C in synthetic air. Thus, a customized debinding and sintering regime was derived. The debinding of the printed components was conducted in an air-ventilated furnace (Xerion, Germany) at several heating rates up to a temperature of 480 °C. During debinding, the furnace was constantly flushed with air at a flow rate of 10 l/min. The sintering of all sample geometries was conducted in an electrical furnace with Kanthal-Super 1800 heating elements with a heating rate of 1 K/min to 460 °C. From 460 °C to 600 °C the heating rate was decreased to 0.5 K/min with the aim to thermally remove last binder portions. Subsequently, the heating rate was set to 3 K/min up to 900 °C and then decreased to 1 K/min up to maximum temperature. The dwell time at the final sintering temperature of 1600 °C was 240 min. Afterwards, a controlled cooling with 1 K/min was conducted. For both thermal treatments, all samples were place on an alumina pebble bed to ensure compensation of the thermal expansion and shrinkage during heat treatment.

Table 1
Initial printing parameters of the M.A.T. 3D printer for bars and plates.

Parameter	Value
Diameter of the nozzle	1.0 mm
Layer width	1.05 mm
Layer height	0.2 mm
Nozzle temperature	210 °C 1st layer, 200 °C 2nd + layer
Bed temperature	60 °C
Printing speed	20 mm/s

The bulk density of the partially debinded samples was determined from weight and volume measurements. The open porosity as well as bulk density of the sintered samples was determined according to DIN EN 993-1 with water as immersion fluid at room temperature. Microstructural characterization of the sintered samples was conducted by scanning electron microscopy (SEM) using an SEM AMBER (Tescan, Czech Republic). Before analyzing, the samples were embedded in epoxy resin and the surface was polished. The modulus of rupture at room temperature was determined according to DIN EN 843-1 using three-point bending tests. Testing was performed on a universal testing machine type TIRA TT 2420 with a 1 kN force transducer. The chosen cross head speed was 1.5 mm/min and the span was 40 mm.

The cylindrical sample with gyroid infill was analyzed with the aid of a microfocus X-ray computed tomography CT-ALPHA (Procon X-Ray, Germany). The tomographic scans were performed with a 160 kV X-ray source and a flat detector Dexela Type 1512 (PerkinElmer, Germany) with 1944 × 1526 active pixel. The reconstructed CT image has a voxel size of 28.97 µm × 28.97 µm x 28.97 µm. The surface of a cube with 15 × 15 mm^2 was evaluated after 3D printing and CNC milling using a VK-X 1000 laser scanning microscope (Keyence Cooperation, Japan). Thermal shock testing of the sintered sheet-gyroid structure was performed according to DIN EN 993-11. The sample were prewarmed at 110 °C and then placed in a furnace at 1100 °C for 45 min to achieve temperature equilibrium. Afterwards, the sheet-gyroid structure was removed from the furnace and quenched by blowing with compressed air (p = 0.1 MPa) for 5 min. This test was repeated 5 times.

3. Results and discussion

3.1. Feed stock preparation and initial printing

Fig. 2 displays the torque-time diagram of the investigated compositions. The compounding process can be divided into three stages. When the mixing of the raw materials begins, a characteristically pronounced increase in torque with peak values between 122 Nm (AT-***10***Cel-10Sa) and 158 Nm (AT-***20***Cel-10Sa) is registered due to particle-particle interactions without a separating binder layer between these particles. These interactions are more pronounced with higher cellulose contents of the binder system since the plasticizing polyethylene content is thereby reduced. In the second stage, particle agglomerates are broken apart and wetted by the binder. Thus, the torque decreases to values between 60 Nm (AT-***10***Cel-10Sa) and 75 Nm (AT-***20***Cel-10Sa). After a mixing time of 14 min, a constant torque for the compositions containing 10 and 15 vol% cellulose is reached, indicating that all ceramic particles are wetted and equilibrium between agglomeration and deagglomeration is obtained. Thus, the flow characteristics are mainly determined by the organic binder, which either forms an interfacial layer on the particle surfaces or fills the spaces between them [29]. For the composition containing 20 vol% cellulose in the binder system, this equilibrium is reached after a mixing time of 18 min.

After compounding of the thermoplastic masses in the Linden kneader and the preparation of the pellets that are exemplarily shown in Fig. 3, bars ($4 \times 5 \times 60$ mm^3) as well as plates ($15 \times 80 \times 2.4$ mm^3) were printed according to the printing parameters listed in Table 1. The simple components printed with M.A.T. pellet printer are shown in Fig. 4.

3.2. Development of the debinding process

The DSC/TG analysis of the binder system, composed of low-density polyethylene, cellulose, stearic acid and ammonium lignin sulfonate, is shown in Fig. 5. It served as an orientation for the thermal debinding regime. Two endothermic peaks can be registered at temperatures of 79.6 °C and 110.5 °C, which correspond to the melting range of stearic acid and polyethylene, respectively. Up to a temperature of 220 °C, a mass loss of 1.59 % was registered due to the evaporation of stearic acid and physically bonded water. The decomposition of the stearic acid starts at 200 °C with a pronounced peak at 279.4 °C. Up to a temperature of 370 °C, a further mass loss of 22.23 % was registered, which was attributed to the complete decomposition of stearic acid and starting decomposition of polyethylene, respectively. The exothermic peaks at 388.0 °C, 459.7 °C and 474.0 °C correspond to the main decomposition reaction of polyethylene and partial decomposition of cellulose. These decomposition reactions are accompanied by a mass loss of 62.12 %. The

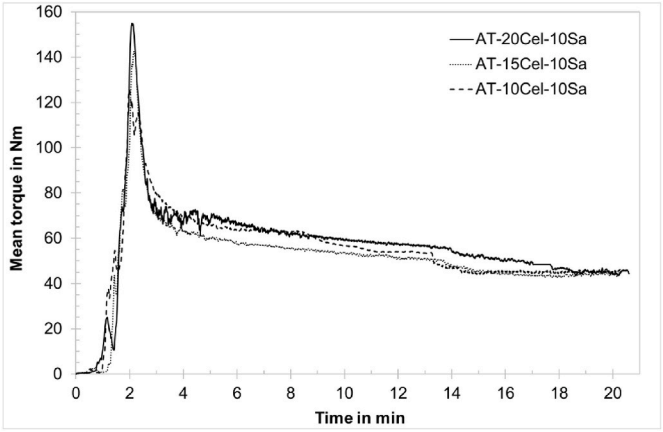

Fig. 2. Variation of torque depending on time and binder composition.

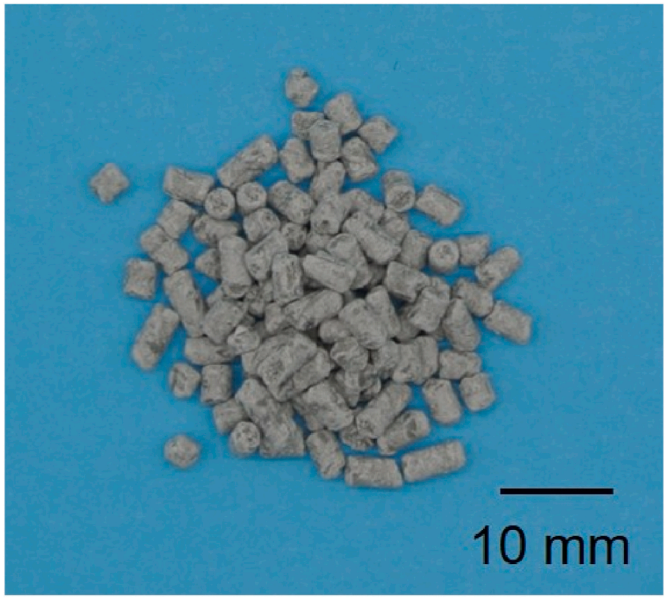

Fig. 3. Pellets of composition AT-20Cel-10Sa after kneader.

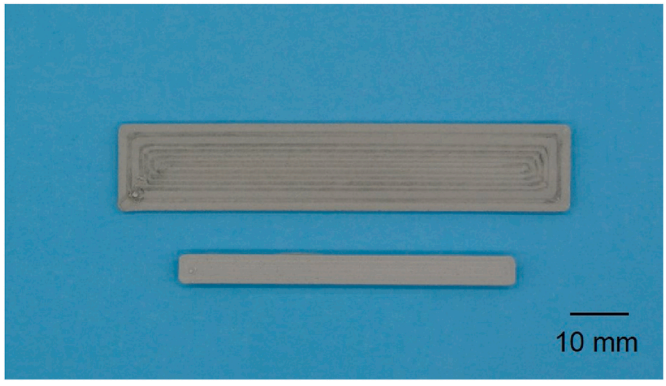

Fig. 4. 3D printed alumina samples using M.A.T. printer, initial printing parameters.

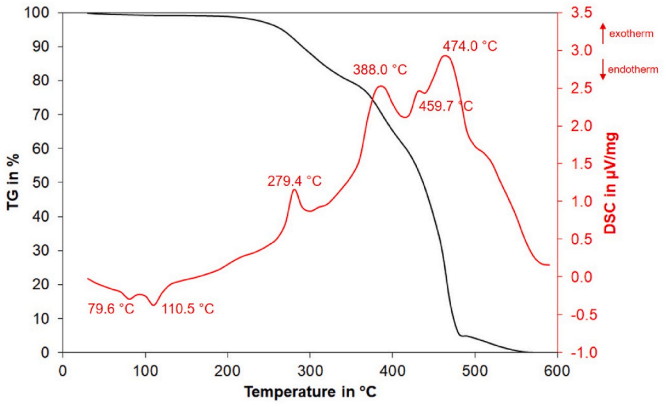

Fig. 5. Thermal analysis of the binder system in synthetic air.

following complete decomposition of the cellulose takes place up to temperatures of 590 °C with a final mass loss of 14.06 %. Thus, during thermal debinding all components of the binder system decompose up to a temperature of 590 °C without residues.

A customized debinding regime was derived with regard to the

results of the DSC/TG analysis, see Table 2. The maximum debinding temperature was set to 480 ° C in order maintain the dimensional stability of the samples, thus allowing the sample transfer from the debinding to the sintering furnace (samples were placed on alumina crucibles and alumina pebble bed). At this stage 5.58 % of cellulose binder remain from the binder system and act as a backbone. The thermal debinding regime contained several dwell times (at 220 °C, 320 °C, 380 °C, 480 °C) in order to achieve temperature equilibrium of the furnace before the main decomposition reactions took place. Contrary to the conventional debinding theory, in which very small heating rates of 0.2 K/min are suggested for materials with a high binder content, a heating rate of 5 K/min was applied in the temperature range between 90 °C and 220 °C. It should be noted, that the DSC/TG analysis indicated no significant decomposition reaction of the single binder components in the temperature range from 90 °C to 220 °C, as the mass loss is minimal (1.5 %). This presented approach is mainly related to the melting of the binder component LDPE in the temperature range between 98 °C and 104 °C and the great risk of pore closure due to liquid binder phase. In the pure thermal debinding, where no additional porosity is generated by wick or solvent debinding, it is of outmost importance to quickly pass through the LDPE melting range. If the limited number of existing cavities between the deposited stands are filled with molten LDPE combined with the formation of a dense skin on the sample surface [5,30], the diffusion of volatiles out of the green body is hindered and results in the formation of bubbles and the swelling of the samples.

During the initial debinding experiments, the formation of bubbles and the swelling of the samples could not be prevented as it is shown in Fig. 6. Consequently, the printing parameters had to be refined to ensure larger cavities and less overlapping between the deposited strand of the printed components. The adjusted printing parameters are summarized in Table 3. The infill density was decreased to 88.7 %, the line height increased to 0.4 mm with the corresponding line width changed to 1.37 mm. The refinement of the printing parameters effectively eliminated the bubble formation and swelling of the debinded samples almost completely. In the middle of the sample, the strands are still narrowly deposited (partly overlapping) since their number is preset by the sample dimensions, the infill and the line width. Hence, few bubbles are formed in the sample middle, indicated with red arrows in Fig. 7.

To eliminate the formation of these small bubbles in the center of the sample, a final adjustment of the printing parameters was carried out. To enable printing from inside to outside and completely avoid strand overlapping, all strands had to be defined as walls (0 % infill). To further provoke cavity formation, the viscosity of the material was increased during printing by reducing the printing temperature to 185 °C from the 2nd layer and above. Applying the final printing parameters, the debinding of all samples including cylinders with gyroid infill as well as sheet-gyroid structures without debinding-related defects was possible. The effect of the applied printing parameter on the print quality and cavity formation is schematically illustrated in Fig. 8.

The dimensional stability of printed components during and after thermal debinding was also of great importance. Therefore, the dimensional stability of extruded rods (100 mm in length) with the different cellulose contents (10–20 vol%) was evaluated. The samples were placed on two alumina bars with a span of 60 mm. The debinding was conducted according to the customized debinding regime displayed in Table 2. Fig. 9 shows selected strands directly after thermal debinding up to 480 °C. Since the samples contained only a small percentage (5.58 %) of the initial binder system (see Fig. 5), they were very fragile and a better illustration could not be achieved. It is shown that a higher cellulose content within the binder system led to a better dimensional stability of the samples with less deformation and crack formation. This can be attributed to the higher decomposition temperature of cellulose compared to the other binder materials [31,32]. The highest thermal stability during and after debinding was found for composition AT-***20***Cel-10Sa. Thus, all following printing experiments were conducted with this material.

Table 2
Customized debinding regime.

Temperature (range) in °C	Heating rate in K/min	Isothermal dwell in min
20–90	1	–
90–220	5	–
220	–	60
220–320	0.5	–
320	–	30
320–380	0.5	–
380	–	30
380–480	0.2	–
480	–	90

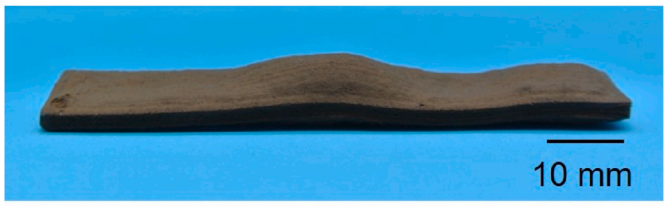

Fig. 6. 3D printed plates after debinding at temperatures of up to 220 °C with a heating rate of 5 K/min, initial printing parameter.

Table 3
Printing parameters utilized within the study.

Parameter	Initial	Intermediate	Final
Layer width	1.05	1.37	1.37
Layer height	0.2	0.4	0.4
Nozzle temperature	210 °C 1st layer, 200 °C 2nd + layer	210 °C 1st layer, 200 °C 2nd + layer	210 °C 1st layer, 185 °C 2nd + layer
Bed temperature	60 °C	60 °C	60 °C
Printing speed	20 mm/s	20 mm/s	20 mm/s
Infill	100 %	88.7	0 % (all walls)
Flow	100 %	90 %	85 %

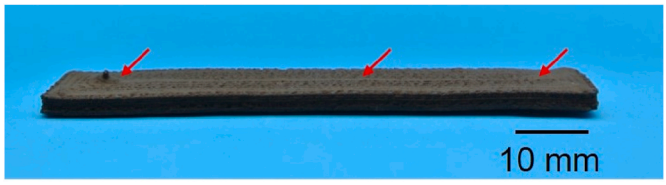

Fig. 7. 3D printed plate after debinding at temperatures of up to 220 °C with 5 K/min, intermediate printing parameters.

In order to verify the reduction of the bubble volume and the swelling of the samples, the bulk densities were determined. Based on the results listed in Table 4, it was observed that a significant increase of the bulk density was provoked by the adjustment of the printing parameters. This means that the fraction of voids in the samples was reduced and the material was denser, showing the success of the developed debinding regime.

3.3. Characterization of the sintered materials (has been shortened)

The SEM images (SE mode) in Fig. 10a and b show the cross-section of the sintered alumina samples printed with the initial (concentrically from outside to inside with a layer height of 0.2 mm, 100 % infill, 100 % flow) and the adjusted final (concentrically from inside to outside with a layer height of 0.4 mm, without infill (all “walls”), 85 % flow) printing

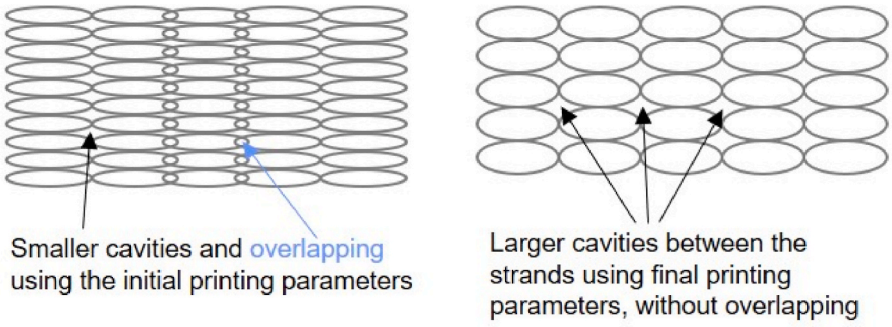

Fig. 8. Scheme of cavity formation depending on applied printing parameter.

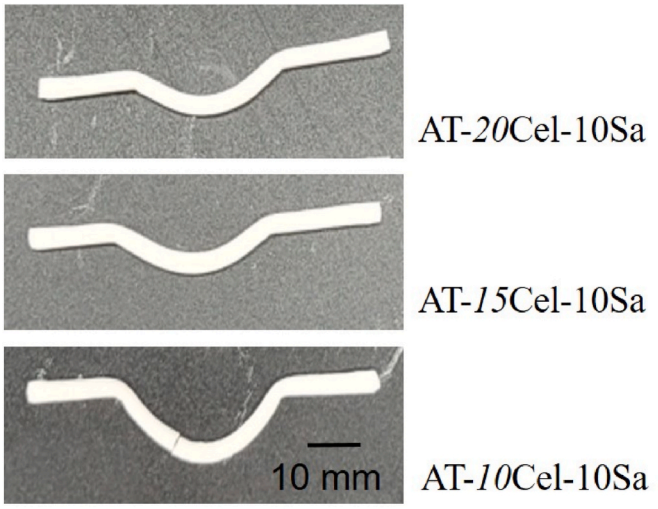

Fig. 9. Results of the thermal stability tests.

Table 4
Bulk density after debinding to 220 °C.

Experiment	Bulk density in g/cm^3
Initial parameters	1.40 ± 0.01 g/cm^3
Intermediate parameters	2.15 ± 0.10 g/cm^3
Final parameters	2.26 ± 0.08 g/cm^3

parameters. Layers printed in vertical z-direction with heights of 200 µm (a) and 400 µm (c) are clearly visible and marked in red. Correlations of the layer height and the size of the cavities are well known [6,7,33]. For the samples prepared with the initial printing conditions, large pores partially filled with epoxy resin are visible in the cross-section, whereas the pores are much smaller for the adjusted printing conditions. For the samples with adjusted final printing parameters it is agreed that the larger layer height led to the formation of larger cavities as compared to the samples with the initial printing parameters. Therefore, an enhanced removal (diffusion) of volatile decomposition products could take place during debinding. Thus, the formation of unwanted bubbles in the final part was prevented and enhanced the connection between neighboring layers during sintering. These findings are in good agreement with the results of the bulk density measurements.

Fig. 11 shows exemplarily a sintered plate and a sintered bar that were prepared using the final printing parameters. The shrinkage for the sintered plates in length and width was determined to be 15.7 ± 0.7 % and 15.1 ± 0.5 %, respectively. The shrinkage for the sintered bars was determined in length to be 14.9 ± 0.4 % and in width to be 13.4 ± 2.1 %. The shrinkage in height was not determined since the samples were slightly deformed. The open porosity as well as the flexural strength of the sintered bars were determined to be 41.3 ± 1.2 % and 50.2 ± 7.7 MPa, respectively. The measured strength of the sintered materials is

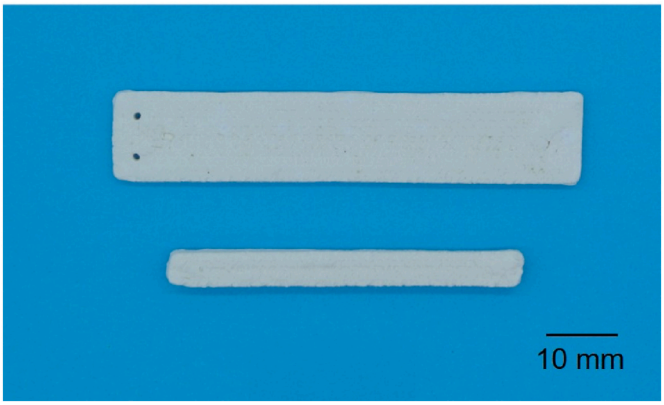

Fig. 11. 3D printed plate after sintering at 1600 °C, final printing parameters.

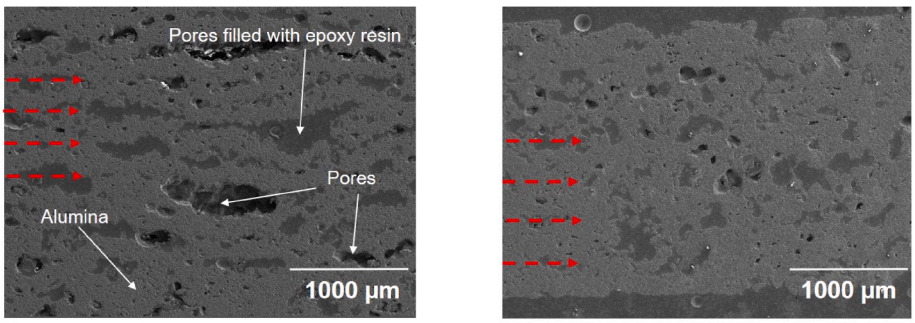

Fig. 10. SEM images (SE-mode) of the sintered alumina plates in cross-sectional view, a) initial printing parameters, b) final printing parameter.

sufficient as porous inert medium, without any load-bearing mechanical function [34–37]. The high open porosity will positively contribute to the thermal shock performance of the components in the novel burners.

3.4. Manufacturing of larger cylindrical components, sheet-gyroid structures and CNC machining of green parts

Cylindrical components with a diameter of 50 mm, a height of 25 mm and a weight of approx. 81 g were printed in 90 min with the optimized printing parameters. The infill densities were 40 % or 44.5 %, respectively. When printing was performed with an infill density of 40 %, holes appeared in the walls throughout the whole part at the saddle points of the gyroid-like structure. The three white markings in Fig. 12a indicate this exemplarily. Using a higher infill density of 44.5 % solved this issue. The printed components were placed on an alumina pebble bed and thermally debinded according to the tailored debinding regime shown in Table 2 with a heating rate of 5 K/min between 90 °C and 220 °C. The structures were subsequently sintered at a maximum sintering temperature of 1600 °C. Fig. 12b shows the cylindrical components after 3D printing and after sintering. Despite the volume shrinkage during debinding, no deformation or crack formation was registered. The total shrinkage after sintering was determined to be 11.3 ± 1.3 % in diameter and 10.7 ± 0.7 % in height. Fig. 13 presents 2D CT-images of the gyroid structure with a voxel size of 28.97 µm after reconstruction in cross-sectional view. The gyroid structure is permeable after sintering and the channels did not close. Nevertheless, there are some minor irregularities. The top part slightly deformed during sintering, thus slightly sunk in. This interfered with the symmetric alignment of the infill strands. In the center of the gyroid structure a higher porosity of the strands can be recognized. The shell also possesses a high, but evenly distributed porosity and also individual strands from the printing process are no longer visible after sintering. The formation of gas bubbles and the swelling during thermal treatment was prevented by applying the precisely optimized printing and debinding parameters.

The sheet-gyroid structures (31.2 × 31.2 × 30 mm^3) were printed with a layer height of 0.4 mm and a random z-seam and a printing temperature of 210 °C in the 1st and then of 185 °C from the 2nd layer and above. Debinding and sintering was conducted using the precisely attuned debinding system. Nevertheless, some printing defects are present in the gyroid structure due to its complex and filigree geometry, which could not always be accurately printed with the 1.0 mm nozzle. In order to reduce the number of defects, the process was then transferred to printing with a 0.4 mm nozzle. The derived final printing parameters shown in Table 3 were directly applicable. Only the line width and the line height had to be adjusted to the new nozzle diameter and were set to 0.45 mm and 0.2 mm, respectively. As a result, defect-free gyroid structures were obtained, showing only minor over-extrusion irregularities. Fig. 14 shows digital images of the sintered and thermally shocked sheet-gyroid structures fabricated with the 1.0 mm and 0.4 mm. Both of the structures successfully survived 5 thermal shock cycles, each involving heating to 1100 °C followed by air quenching, which is an excellent result in terms of thermal shock performance.

In a final experiment, the CNC-machinability of the developed binder system was tested on printed alumina components with the composition AT-20Cel-10Sa. Cubes with an edge length of 18 mm were printed with the optimized printing parameters and immediately CNC-milled with a spindle rotation of 9000 rpm, a processing speed of 650 mm/min and a cutting depth of 0.1–0.3 mm. Fig. 15a displays a digital image of a

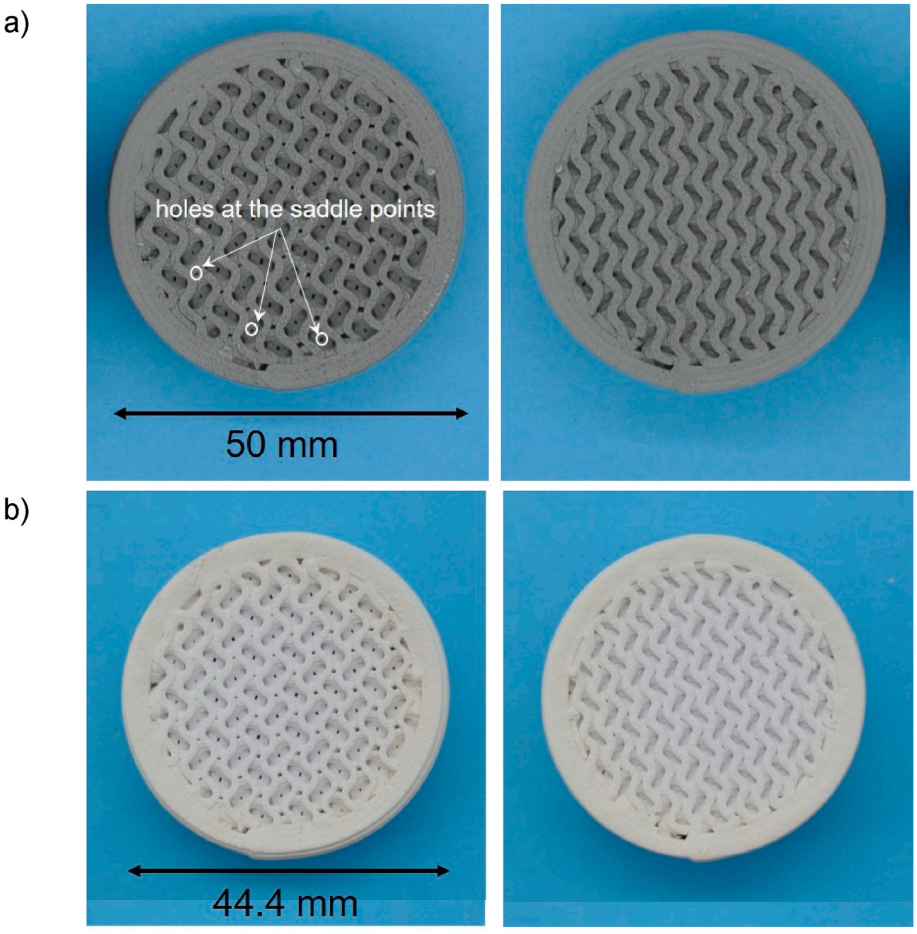

Fig. 12. Gyroid-like porous (left) and gyroid (right) structures a) as printed, b) printed, debinded and sintered state.

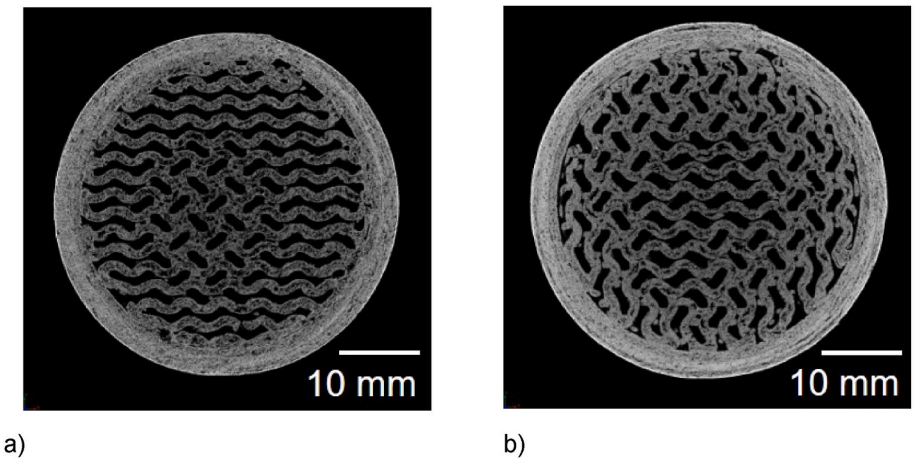

Fig. 13. 2D-CT images of the sintered gyroid structure (cross-section), a) top, b) bottom.

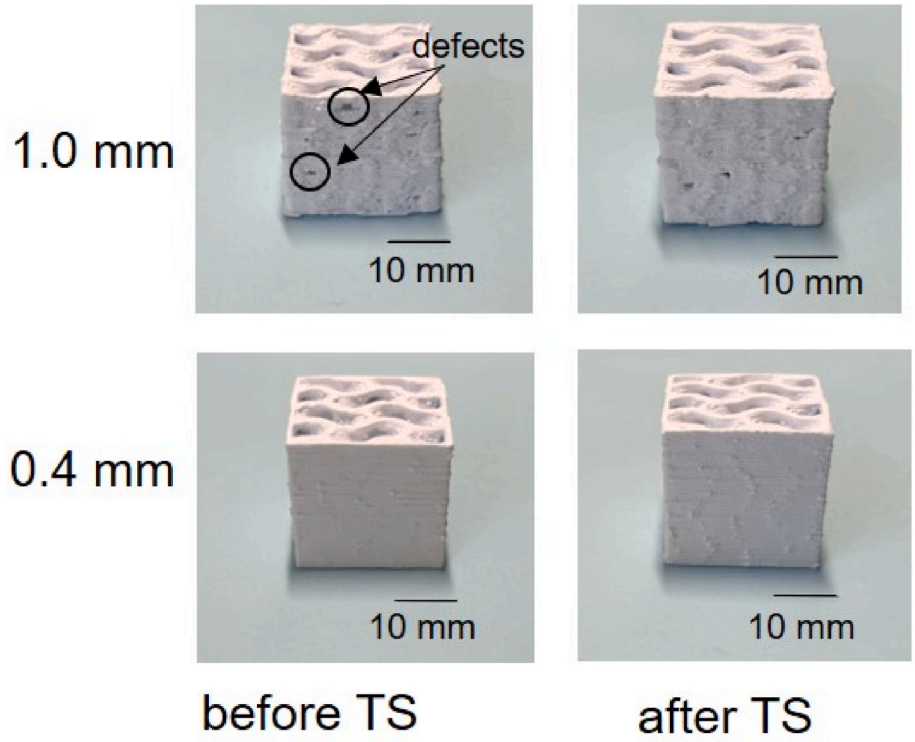

Fig. 14. Sheet-gyroid structures a) after sintering and b) after 5 thermal shock cycles.

machined cube. There are several benefits that have been observed. There are no signs of melt formation, which proves the good resistance of the binder system to heat and thus to warping. Since the bed is heated during printing, the components are slightly wider and denser in the bottom part. The CNC-milling allowed to significantly improve the dimensional precision of the parts., The colored topographic maps show the height differences in the sample surface in printed (Fig. 15b) and CNC-machined (Fig. 15c) state. While the height difference is approx. 330 µm in the unmachined sample, it was reduced to approx. 200 µm due to CNC-machining. Thus, removing excess material as well as printing irregularities led to an improved surface quality.

4. Conclusion

Within the present complex components in gyroid structure based on alumina were fabricated using 3D fused granulate fabrication. The developed components are integral part of novel burners designed for the non-premixed combustion of ammonia.

Starting from the raw materials, the fabrication routine for pellets with special regard to the binder system was developed. The pellets with a alumina to binder ratio of 52 vol% : 48 vol% were directly applied for component printing without further processing steps.

A customized debinding regime that utilizes purely the thermal decomposition reactions of the binder components without wick or solvent debinding was presented. Challenges regarding this debinding strategy such as sample swelling and bubble formation were successfully addressed through a stepwise adjustment of the printing parameters due to the specific introduction of interstrand cavities.

The determined strength of the sintered materials was 50.2 ± 7.7 MPa and is more than sufficient for the intended application at elevated temperatures and thermal shock load. Moreover, the high open porosity 41.3 ± 1.2 % positively contributed to the thermal shock performance of

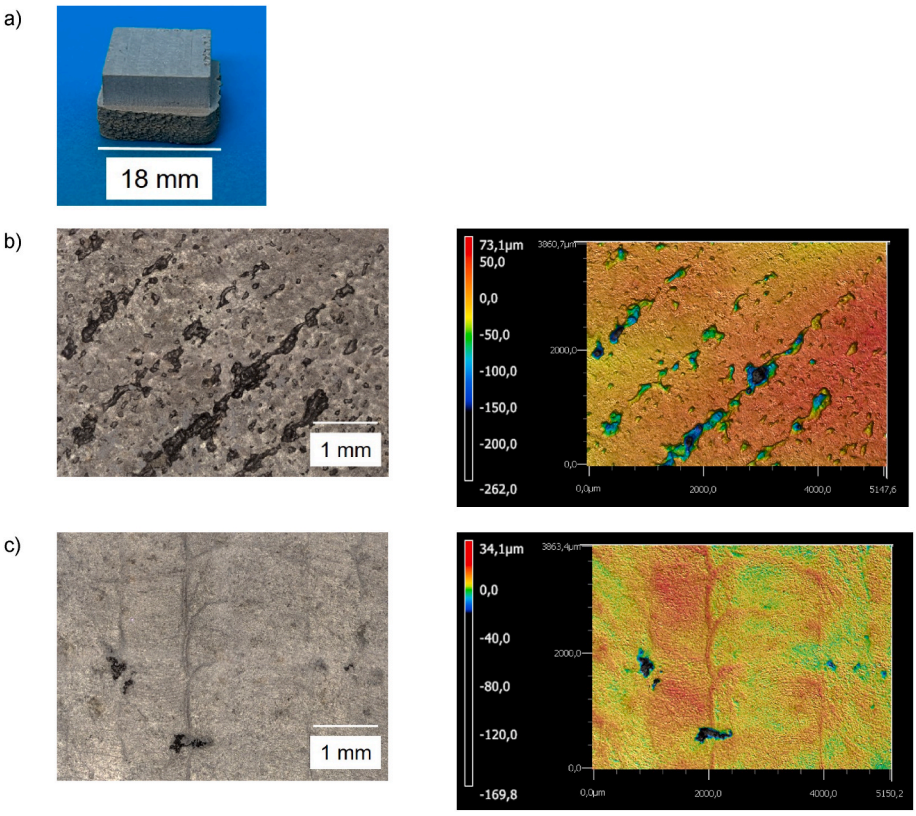

Fig. 15. CNC-machined cube in green state, a) green component, b) bottom side, c) machined top surface with circular lines due to rotating CNC-tool. (For interpretation of the references to color in this figure legend, the reader is referred to the Web version of this article.)

the components in the novel burners.

Larger cylindrical components with gyroid infill with a diameter of 50 mm and a height of 25 mm were successfully fabricated using the elaborated parameters for printing, debinding and sintering. Their shrinkages in diameter and height after sintering were determined to be 11.7 ± 1.3 % and 10.7 ± 0.7 %, respectively.

Sheet-gyroid structures were prepared using 1.0 mm as well as 0.4 mm printing nozzle. The printing, debinding and sintering process was successfully transferred to printing with smaller nozzle diameter, showing the excellent versatility of the developed process technology. The sintered sheet-gyroid structures successfully survived 5 thermal shock cycles, each involving heating to 1100 °C followed by air quenching, which is an excellent result in terms of thermal shock performance.

Due to the direct CNC-machining of printed components prepared with the developed feedstock a high quality of the surfaces could be achieved.

In future work, the successfully developed sheet-gyroid structures will be further characterized and tested in combustion atmosphere.

CRediT authorship contribution statement

Claudia Heuer: Writing – review & editing, Writing – original draft, Resources. **Benjamin Bock-Seefeld:** Writing – review & editing, Resources, Data curation. **Patricia Kaiser:** Writing – review & editing, Resources. **Christian Weigelt:** Writing – review & editing. **Piotr Malczyk:** Writing – review & editing. **Nora Brachhold:** Writing – review & editing, Funding acquisition. **Dimosthenis Trimis:** Supervision, Funding acquisition. **Christos G.C. Aneziris:** Writing – review & editing, Supervision, Funding acquisition.

Declaration of competing interest

The authors declare that they have no known competing financial interests or personal relationships that could have appeared to influence the work reported in this paper.

Acknowledgements

The authors gratefully acknowledge the financial support of the Deutsche Forschungsgemeinschaft (DFG, German Research Foundation) for funding this research project within the frame of the DFG Priority Program 2419 HyCAM– project number 523876164. The authors would like to acknowledge the support of Dr.-Ing. Jana Hubalkova and Dr.-Ing. Claudia Voigt for performing CT- and surface analyses.

References

[1] S. Publishing, Ceramics Additive Manufacturing Production Markets: 2019-2030, 2020.
[2] W. Kollenberg, Additive Fertigung Keramischer Komponenten: Grundlagen Und Anwendungen, 1. Auflage ed., Vulkan Verlag, Essen, 2020.
[3] AM Editorial Team, 3D printing with plastic pellets - what you need to know, additive manufacturing, in: Additive Manufacturing Media, 2023. Cincinnati, Ohio, United States.
[4] V. Truxová, J. Šafka, J. Sobotka, J. Macháček, M. Ackermann, Alumina manufactured by fused filament fabrication: a comprehensive study of mechanical properties and porosity, Polymers 14 (2022) 991.
[5] L. Gorjan, C. Galusca, M. Sami, T. Sebastian, F. Clemens, Effect of stearic acid on rheological properties and printability of ethylene vinyl acetate based feedstocks for fused filament fabrication of alumina, Addit. Manuf. 36 (2020) 101391.
[6] D. Nötzel, R. Eickhoff, T. Hanemann, Fused filament fabrication of small ceramic components, Materials 11 (2018) 1463.
[7] D. Nötzel, R. Eickhoff, C. Pfeifer, T. Hanemann, Printing of Zirconia parts via fused filament fabrication, Materials 14 (2021) 5467.
[8] A. Hadian, M. Fricke, A. Liersch, F. Clemens, Material extrusion additive manufacturing of zirconia parts using powder injection molding feedstock compositions, Addit. Manuf. 57 (2022) 102966.

[9] H. Masuda, Y. Ohta, M. Kitayama, Additive manufacturing of SiC ceramics with complicated shapes using the FDM type 3D-Printer, J. Mater. Sci. Chem. Eng. 7 (2019) 1–12.
[10] S. Danforth, Fused deposition of ceramics: a new technique for the rapid fabrication of ceramic components, Mater. Technol. 10 (1995) 144–146.
[11] B. Akhoundi, F. Sousani, An experimental investigation of screw-based material extrusion 3D printing of metallic parts, J. Eng. Res. 12 (2024) 226–232.
[12] T. Sangkharat, L. Techawinyutham, Development of screw-based 3D printing machine and process experiments for short fiber reinforced polymer composites, Appl. Sci. Eng. Prog. 17 (2024).
[13] A. Smirnov, S. Terekhina, T. Tarasova, L. Hattali, S. Grigoriev, From the development of low-cost filament to 3D printing ceramic parts obtained by fused filament fabrication, Int. J. Adv. Des. Manuf. Technol. 128 (2023) 511–529.
[14] C. de la Torre-Gamarra, M.D. García-Suelto, D. del Rio Santos, B. Levenfeld, A. Varez, 3D-printing of easily recyclable all-ceramic thick $LiCoO_2$ electrodes with enhanced areal capacity for Li-ion batteries using a highly filled thermoplastic filament, J. Colloid Interface Sci. 642 (2023) 351–363.
[15] P. Veteška, Z. Hajdúchová, J. Feranc, K. Tomanová, J. Milde, M. Kritikos, L. Bača, M. Janek, Novel composite filament useable in low-cost 3D printers for fabrication of complex ceramic shapes, Appl. Mater. Today 22 (2021) 100949.
[16] Y. Zhu, F. Liu, Y. Wang, H. Zhang, P. Xue, L. Wu, D. Ni, B. Xiao, Z. Ma, Fabrication of thin-walled metal structures with enhanced energy absorption capabilities by metal-fused deposition modeling without using debinding chemical reagents, Adv. Eng. Mater. 27 (2025) 2402792.
[17] A. Cherouat, T. Barriere, H. Wang, Experimental analysis of extrusion-based additive manufacturing process of bio-composite NiTi alloy, Int. J. Damage Mech. 34 (2025) 573–597.
[18] Y.F. Zhu, F.C. Liu, Y.D. Wang, H. Zhang, P. Xue, Z. Zhang, L.H. Wu, D.R. Ni, B. L. Xiao, Z.Y. Ma, Investigation on energy absorption characteristics of thin-walled structures fabricated by bound metal deposition without using debinding chemical reagents, J. Mater. Res. Technol. 35 (2025) 2263–2271.
[19] P. Gehre, C.G. Aneziris, EBSD- and CT-analyses for phase evolution and crack investigations of thermal shocked flame sprayed alumina and alumina-rich structures, Ceram. Int. 37 (2011) 1731–1737.
[20] S. Yaroshevskyi, P. Malczyk, C. Weigelt, J. Hubalkova, S. Dudczig, U. Lohse, C. G. Aneziris, Fused filament fabrication of thermal-shock resistant fine-grained refractories for steel-casting applications, Ceramics 6 (2023) 475–491.
[21] M.S. Crowley, Hydrogen-silica reactions in refractories, Ceramic Bull. 46 (1967) 679–682.
[22] Z. Guo, J. Li, M. Zhao, J. Cao, Y. Zhang, X. Lu, D. Zhang, Effect of bed material on ammonia dissociation in a bubbling fluidised bed, Int. J. Hydrogen Energy 119 (2025) 444–456.
[23] S.R. Holden, Z. Zang, J. Wu, D. Zhang, Ammonia combustion in fix-bed and fluidised-bed reactors: the concept, knowledge base, and challenges, Prog. Energy Combust. Sci. 109 (2025) 101230.
[24] G. Brenner, K. Pickenäcker, O. Pickenäcker, D. Trimis, K. Wawrzinek, E. Weber, Numerical and experimental investigation of matrix-stabilized methane/air combustion in porous inert media, Combust. Flame 123 (2000) 201.
[25] P. Weinbrecht, B. Stelzner, P. Habisreuther, C. Weis, D. Trimis, Experimental investigation of irradiance from combustion in porous media with different geometries, Appl. Energy Combust. Sci. 20 (2024) 100294.
[26] e.V. Deutsches Institit für Normung, Determination of the melt mass-flow rate (MFR) and melt volume-flow rate (MVR) of thermoplastics - part 1: standard method. DIN EN ISO 1133-1:2022, Beuth Verlag GmbH, Berlin, 2022.
[27] O. Al-Ketan, R.K.A. Al-Rub, MSLattice: a free software for generating uniform and graded lattices based on triply periodic minimal surfaces, Mater. Design Process. Commun. 3 (2021) e205.
[28] J. Riegel, W. Mayer, Y. van Havre, Freecad, 2001-2023. Version 0.21.2) [Software].
[29] T. Hanemann, R. Heldele, T. Mueller, J. Hausselt, Influence of stearic acid concentration on the processing of ZrO_2-Containing feedstocks suitable for micropowder injection molding, Int. J. Appl. Ceram. Technol. 8 (2011) 865–872.
[30] J.E. Zorzi, C.A. Perottoni, J.A.H. Da Jornada, Hard-skin development during binder removal from Al_2O_3-based green ceramic bodies, J. Mater. Sci. 37 (2002) 1801–1807.
[31] C. Aneziris, S. Yaroshevskyi, P. Malczyk, Filaments for the thermoplastic 3D production of ceramic components, metallic components or components based on metal-ceramic composites or material composites, in: Deutsches Patent und Markenamt, WO2023186645A1, 2023.
[32] L. Szczésniak, A. Rochocki, J. Tritt-Goc, Glass transition temperature and thermal decomposition of cellulose powder, Cellulose 15 (2008) 445–451.
[33] V.E. Kuznetsov, A.N. Solonin, A. Tavitov, O. Urzhumtsev, A. Vakulik, Increasing strength of FFF three-dimensional printed parts by influencing on temperature-related parameters of the process, Rapid Prototyp. J. 26 (2020) 107–121.
[34] J. Chen, X. Liang, Y. Li, Z. Wu, Q. Wang, L. Pan, S. Sang, Preparation and properties of alumina reticulated porous ceramics for high-temperature porous medium combustion, Ceram. Int. (2025).
[35] M. Fukushima, A. Shimamura, P. Colombo, H. Hyuga, T. Ohji, Y.-I. Yoshizawa, Porous ceramics processing, in: M. Pomeroy (Ed.), Encyclopedia of Materials: Technical Ceramics and Glasses, Elsevier, Oxford, 2021, pp. 342–345.
[36] C. Voigt, T. Zienert, P. Schubert, C.G. Aneziris, J. Hubálková, Reticulated porous foam ceramic with different surface chemistries, J. Am. Ceram. Soc. 97 (2014).
[37] C.G. Gumban, J. Hubálková, M. Neumann, E. Werzner, A. Charitos, C.G. Aneziris, C. Voigt, Thermal shock resistance of industrial foam filters - a comparative study, Open Ceramics 16 (2023).